DOI: 10.1002/cssc.201702068

Tracking Ionic Rearrangements and Interpreting Dynamic Volumetric Changes in Two-Dimensional Metal Carbide Supercapacitors: A Molecular Dynamics Simulation Study

Kui Xu,[a, b, c] Zifeng Lin,[a, c] Céline Merlet,[a, c] Pierre-Louis Taberna,[a, c] Ling Miao,[b] Jianjun Jiang,*[b] and Patrice Simon*[a, c]

We present a molecular dynamics simulation study achieved on two-dimensional (2D) $Ti_3C_2T_x$ MXenes in the ionic liquid 1-ethyl-3-methylimidazolium bis(trifluoromethylsulfonyl)imide ($[EMIM]^+[TFSI]^-$) electrolyte. Our simulations reproduce the different patterns of volumetric change observed experimentally for both the negative and positive electrodes. The analysis of ionic fluxes and structure rearrangements in the 2D material provide an atomic scale insight into the charge and discharge processes in the layer pore and confirm the existence of two different charge-storage mechanisms at the negative and positive electrodes. The ionic number variation and the structure rearrangement contribute to the dynamic volumetric changes of both electrodes: negative electrode expansion and positive electrode contraction.

Introduction

Nowadays, there is a rising demand for reliable and safe energy-storage technologies, such as for (hybrid) electrical vehicles, portable electronic devices, and smart grids. Thus, high-performance electrochemical energy storage devices are needed. An increasing number of materials-driven research aims at boosting the energy, power density, and cycle life of rechargeable batteries or at increasing the energy density of electrochemical capacitors.[1] The discovery of two-dimensional (2D) layered materials as host structures for ion intercalation reactions yielded tremendous attention during the past decade.[2] These 2D nanomaterials, which include graphene, transition-metal oxides, transition-metal dichalcogenides,[3] or transition-metal carbides and nitrides (MXenes), have demonstrated promising performances as electrode materials for rechargeable batteries and supercapacitors.[4]

[a] K. Xu, Dr. Z. Lin, Dr. C. Merlet, Dr. P.-L. Taberna, Prof. P. Simon
CIRIMAT UMR CNRS 5085
Université Paul Sabatier Toulouse III
118 route de Narbonne
31062 Toulouse (France)
E-mail: simon@chimie.ups-tlse.fr

[b] K. Xu, Prof. L. Miao, Prof. J. Jiang
School of Optical and Electronic Information
Huazhong University of Science and Technology
Wuhan, Hubei 430074 (P.R. China)
E-mail: jiangjj@mail.hust.edu.cn

[c] K. Xu, Dr. Z. Lin, Dr. C. Merlet, Dr. P.-L. Taberna, Prof. P. Simon
FR CNRS 3459
Réseau sur le Stockage Electrochimique de l'Energie (RS2E)
33 rue Saint Leu
80039 Amiens (France)

Supporting Information for this article can be found under: https://doi.org/10.1002/cssc.201702068.

This publication is part of a Special Issue on Interfacing Theory and Experiment for the Development of Energy Materials.
Please visit the issue at http://doi.org/10.1002/cssc.v11.12.

2D nanomaterials possess a high specific surface area; they store the energy by a fast ion intercalation/deintercalation mechanism between the layers without phase transformation, thus providing intercalation pseudocapacitance.[5] This mechanism is associated with rapid expansion and contraction of the multi-layer 2D materials.[6] Unlike rigid 3D structures, the flexible nature of 2D materials,[7] which is free to expand and contract, favors a fast ion transport inside the 2D interlayer spacing that makes these materials suitable for high-power applications.

One of the key challenges in exploiting the full potential of these 2D materials is to understand the charge-storage mechanism occurring inside the 2D slit-shaped nanopores present in these materials during the electrochemical process. Although considerable efforts have been made to understand the relation between the morphology/architecture and the electrochemical performance of 2D nanomaterials using conventional electrochemical techniques (voltammetry, galvanostatic experiments, electrochemical impedance spectroscopy, etc.),[4a] less attention has been paid to the in situ dynamic behavior during the electrochemical process. As there are still many technological difficulties to achieve a direct quantification of the species population and dynamics on the molecular scale, it is challenging to probe ion dynamics in working electrodes.

Recently, some in situ characterization techniques were developed to tackle this problem. Griffin and co-workers directly quantified the populations of anions and cations[8] and observed the ion dynamics[9] inside a system resembling a 2D material—a microporous carbon electrode. To this end, they used in situ nuclear magnetic resonance (NMR) spectroscopy combined with electrochemical quartz crystal microbalance (EQCM) gravimetry. Their results revealed different charge-storage mechanisms for the positive and negative electrodes. For the system they studied, a tetraethylphosphonium tetrafluorobo-

rate/acetonitrile electrolyte in contact with activated carbon electrodes, they observed that under negative polarization the charge is stored by counter-ion (cation) adsorption whereas for positive polarization an ion exchange mechanism dominates. Furthermore, Tsai et al.[10a] and Levi et al.[10b,c] reported the sensitive probing of dynamic composition changes in porous carbon electrodes under charging by gravimetric analysis using EQCM.

MXenes are 2D materials first reported by Naguib et al.[11] MXenes show 2D morphology,[12] ion-intercalation capacity,[5a,b] metallic conductivity, and tunable surface terminations;[13] these properties make them promising materials for energy storage[4b] and other applications including electrochemical capacitors,[14] Li-ion batteries,[15] and actuators.[6a,16] In previous studies, we investigated the intercalation and deintercalation of 1-ethyl-3-methylimidazolium ($[EMIM]^+$) cations and/or bis(trifluoromethylsulfonyl)imide ($[TSFI]^-$) anions in the MXene $Ti_3C_2T_x$ (T_x stands for various surface terminations (OH, O, and/or F groups) here) electrode and observed the associated volumetric dynamic changes using in situ X-ray diffraction.[6b] Later, Jäckel et al. further explored the swelling/contraction of the same $Ti_3C_2T_x$ MXene in contact with different ionic liquids during electrochemical cycling using both electrochemical dilatometry and in situ X-ray diffraction measurements.[16] These two studies evidenced a volume expansion at the negative polarization and a contraction at the positive electrode during constant-current charge. However, the mechanism at the origin of the charge storage in these neat ionic liquids is still unclear.

In this paper, we propose an atomistic interpretation of the volumetric change by tracking the ionic rearrangement in $Ti_3C_2T_x$ MXene using molecular dynamics (MD) simulations. MD simulations play an important role in understanding the dynamics of charging in nanoporous supercapacitor electrodes.[17] We develop a flexible simulation system with multi-layered MXene electrodes immersed into a neat ionic liquid electrolyte. In contrast to previous studies,[18] the MXene electrode layers are set movable during the simulation process. We are thus able to track the evolution of some characteristic quantities, such as the displacement of the MXene layers, the change of the in-pore ion numbers, and the electric double layer structures inside nanopores as a function of time.

Results and Discussion

A snapshot of the simulation system is shown in Figure 1. Two four-layer $Ti_3C_2T_x$ electrodes were immersed in $[EMIM]^+[TFSI]^-$ ionic liquid electrolyte. The $Ti_3C_2T_x$ MXene electrodes and the $[EMIM]^+[TFSI]^-$ ionic liquid electrolyte were selected according to our previous work.[6b] The $Ti_3C_2T_x$ MXene layers were decorated with three different functional groups (T denotes –F, =O, –OH).[20] Three independent systems ($Ti_3C_2OH_2$, $Ti_3C_2O_2$, $Ti_3C_2F_2$) were used to investigate the effect of these different functional groups. The multilayered $Ti_3C_2T_x$ with an initial interlayer spacing of 1.0 nm were set flexible; each $Ti_3C_2T_x$ layer could move independently as a rigid body during the simulation. The ionic-liquid ions uniformly surrounding the outer surface of the electrode spontaneously intercalated into the interlayer spacing during the equilibration run without any external polarization.

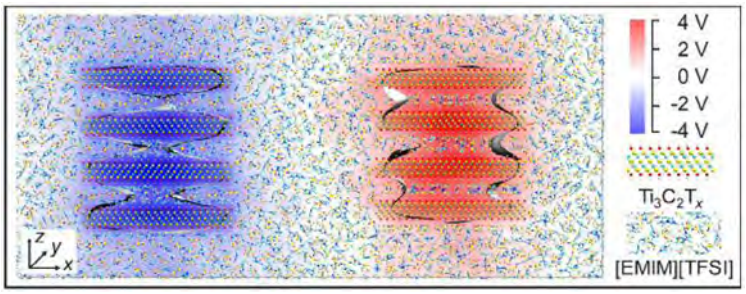

Figure 1. Snapshot of the simulation system obtained using the VMD software.[19] The system consists of a negative electrode (four layers of $Ti_3C_2T_x$ on the left), a positive electrode (four layers of $Ti_3C_2T_x$ on the right), and a pure ionic liquid ([EMIM][TFSI]) surrounding the electrodes. The color spectrum, with blue as the lowest electrostatic potential value and red as the highest, is employed to convey the varying intensities of the electrostatic potential values. The silvery wavy surfaces surrounding the $Ti_3C_2T_x$ layers represent the electrostatic isopotential surfaces of −2 (negative electrode) and +2 V (positive electrode).

The simulations began with a no external polarization equilibrium run. After the simulated systems reached equilibrium, a galvanostatic charge–discharge process was simulated. The variation mode of the extra charge on the negative and positive electrodes as a function of the simulation time is represented in Figure 2a. When charging, the left $Ti_3C_2T_x$ electrode was progressively charged with a constant negative extra charge ($-\Delta q_e$) until the maximum charged value $-q_e$ was reached while the right $Ti_3C_2T_x$ electrode was charged with an equivalent constant positive extra charge (Δq_e). The electrical neutrality is thus maintained in the entire system during the simulation.

Upon charging, the electrostatic potential of the left $Ti_3C_2T_x$ electrode decreases whereas the electrostatic potential of the right $Ti_3C_2T_x$ electrode increases; a potential drop is observed between the two electrodes, coming from the electrolyte ionic resistance. The electrostatic potential difference drives the ion mobility and rearrangement inside/outside the pore. The electrostatic potential map of the modeled system at the maximum charged state, as a result of rearrangements of the electrolyte ions, is calculated using the PME plugin of VMD[21] and represented in Figure 1. The nearly 0 V potential zone (white color zone of the potential map) is reached in the middle region between the two electrodes, thus proving that the electrostatic equilibrium is reached in the simulation system when charged. The electrostatic isopotential surfaces with values of −2 and 2 V are shown, surrounding the negative $Ti_3C_2T_x$ surface and the positive $Ti_3C_2T_x$ surface, respectively. The ≈4 V potential drop observed between the two electrodes is in line with experimental values.[6b]

Electrode volumetric dynamic

The change of the interlayer distance between the $Ti_3C_2T_x$ layers, which directly reflects the variation of electrode volume,

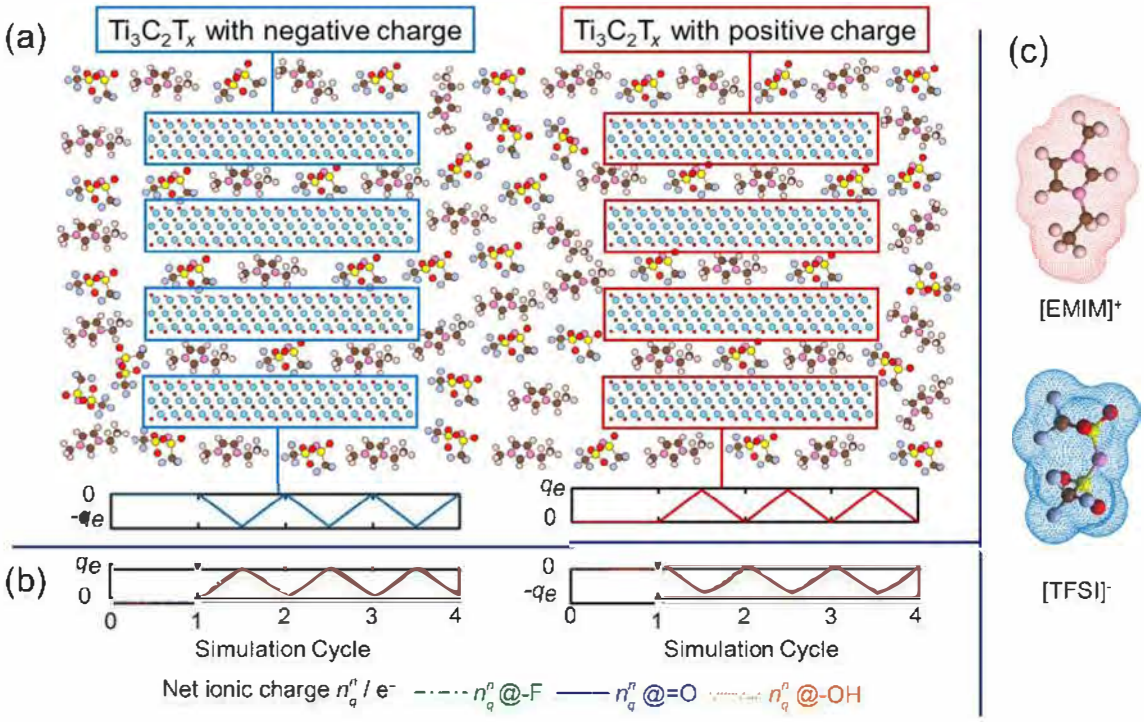

Figure 2. (a) Schematic of the variation of the extra charge amount on the $Ti_3C_2T_x$ layer as a function of the simulation time on the negative and positive electrodes. (b) Variation of the net ionic charge $\Delta n_q^{\text{in pore}}$ in the pores of both the negative electrode and the positive electrode with different functional groups (–F, =O, –OH) during the neutral cycle (0–1 cycle) and galvanostatic charge–discharge cycles (1–4 cycles). (c) Schematic of the atomic structure of $[EMIM]^+$ and $[TFSI]^-$ ions and their occupied volume.

is simulated first. Figure 3 shows the average interlayer distances between the $Ti_3C_2T_x$ layers at both negative and positive electrodes during open-circuit voltage (OCV, 0 to 1 cycle) and galvanostatic charge–discharge cycles (cycle 1–4). During the equilibration cycle at OCV, the $Ti_3C_2T_x$ interlayer distances slightly deviate from their initial values and reach new stable values. Because of the different van der Waals (vdW) and coulombic interactions between the ions and the electrode surface, the in-pore ions form different stable layered structures to reach minimum energy states inside the pore. The different functional groups thus lead to different interlayer distances. The new stable average interlayer distances are ≈0.96, ≈0.82, and ≈0.91 nm for $Ti_3C_2F_2$, $Ti_3C_2O_2$, and $Ti_3C_2OH_2$ electrodes, respectively.

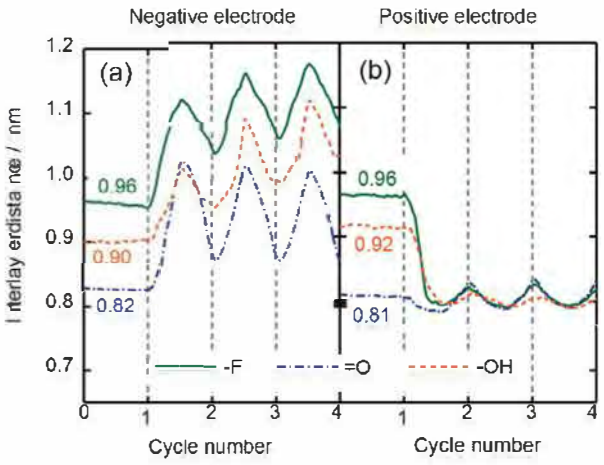

Figure 3. Evolution of the average interlayer distances between the $Ti_3C_2T_x$ layers of both negative and positive electrode during the neutral cycle (0–1 cycle) and galvanostatic charge–discharge cycles (1–4 cycles). A simulation result for nine galvanostatic charge–discharge cycles is shown in Figure S3 in the Supporting Information.

The interlayer distance follows opposite trends during the charge–discharge cycles, depending on electrode polarity. During charging, Figure 3 shows a reversible, continuous expansion of the $Ti_3C_2T_x$ interlayer distance at the negative electrode while a reversible, continuous contraction is observed at the positive electrode. At the negative electrode side, the interlayer distance reaches its maximum value at the fully charged state and continuously decreases during discharge. The minimum value of the interlayer distance after the first discharge is slightly different from the initial one (about 5% larger). At the positive electrode, the opposite trend is observed: the interlayer distance drops to a minimum value at the fully charged state and then slightly increases upon discharge. The new neutral state values of $Ti_3C_2T_x$ with different functional groups deviate considerably from their initial values at OCV and are similar to each other. The dynamic qualitative changes of the interlayer distance at both negative and positive electrodes are consistent with our previous in situ XRD experimental observations.[6b] Finally, Figure 3 shows that there is an irreversible increase (decrease) of about 10% of the interlay-

er spacing during the first cycle at the negative (positive) electrode.

Furthermore, although the nature of the functional groups present on the $Ti_3C_2T_x$ surface does not affect the general trend, it has an impact on the amplitude of the interlayer distance change. After the first cycle, the amplitude of the change upon cycling is smaller at the positive electrode (about ± 0.03 nm) than that observed at the negative electrode (about ± 1 nm). In addition, the variation of the interlayer distances during charge–discharge does not depend on the nature of the surface group at the positive electrode, different from the negative side. This difference may come from the ion arrangement inside the pore; this will be discussed below. The average expansion rates normalized to the equilibrium distance measured at OCV are 9.0–17.0% with different functional groups at the negative electrode whereas the contraction rates are only 2.5%–5.0% at the positive electrode. The calculated changes agree well with those observed during in situ XRD tracking and chronoamperometric dilatometry measurements with the $Ti_3C_2T_x$ MXene: a maximum expansion of 9% at -1.0 V and a maximum contraction of 1% at $+0.5$ V were observed.[16]

Change of ion population in the electrodes

To further clarify the charge storage mechanisms responsible for the volumetric change of the $Ti_3C_2T_x$ electrodes, the evolution of the net ionic charge $n_q^{\text{in pore}}$ (calculated using $n_q^{\text{in pore}} = n_+^{\text{in pore}} - n_-^{\text{in pore}}$, where $n_+^{\text{in pore}}$ and $n_-^{\text{in pore}}$ are the in-pore numbers of $[EMIM]^+$ and $[TFSI]^-$, respectively) and in-pore $[EMIM]^+$ and $[TFSI]^-$ ion populations were calculated and are shown in Figure 2b and Figure 4, respectively. The net ionic charge balances most of the injected charges in the electrode in real time, at both electrodes ($\approx$93.5% in negative and $\approx$90.3% in positive electrode). The nature of the functional groups does not significantly impact the charge compensation, the in-pore net ionic charge being nearly the same with different functional groups. It can be concluded that the extra electrostatic interaction dominates the ion transfer rather than the coulombic and vdW interactions resulting from the presence of surface functional groups.

The change in the in-pore net ionic charge results from the counter-ion and co-ion intercalation/deintercalation between the $Ti_3C_2T_x$ layers. In the negative electrode, there is a clear increase (decrease) of the number of counter ions $[EMIM]^+$ and a slight decrease (increase) of the co ions $[TFSI]^-$ during the charging (discharging) process. It can be concluded that the extra charge on the electrode is mainly compensated by counter-ion intercalation. On the other hand, the positive electrode exhibits a slightly higher extent of co-ion deintercalation than counter-ion intercalation during charging, leading to an ion exchange—or swapping—mechanism. Interestingly, these simulation patterns at both negative and positive electrodes are similar to the ones observed by in situ NMR spectroscopy in microporous carbon pores in the range -1.5 to $+1.5$ V.[8]

Considering the change of in-pore co-ion number $\Delta n_{\text{co ion}}^{\text{in pore}}$ and counter-ion number $\Delta n_{\text{counter ion}}^{\text{in pore}}$ calculated from the simulation trajectories, various charge-storage mechanisms are possible to compensate Δq_e, the extra charge on the electrode. We have followed the approach suggested in previous studies to classify these mechanisms into three categories: i) counter-ion intercalation: the charging process is entirely driven by the adsorption of the counter ion into the pore ($\Delta q_e = \Delta n_{\text{counter ion}}^{\text{in pore}}$); ii) co-ion deintercalation: the charging is driven by the desorption of co ions ($\Delta q_e = -\Delta n_{\text{co ion}}^{\text{in pore}}$); and iii) co-ion/counter-ion exchange: charge is balanced by counter-ion adsorption and co-ion desorption simultaneously ($\Delta q_e = \Delta n_{\text{counter ion}}^{\text{in pore}} - \Delta n_{\text{co ion}}^{\text{in pore}}$).[22] A charging may involve a combination of the different mechanisms in practice. Based on this, we evaluated the proportion of each mechanism at the negative electrode and positive electrode and represent it in Figure 5. In the negative electrode, we calculated that the extra electrode charge q_e is mainly compensated by counter-ion intercalation (68.7% up to 94.7%) and only 6.3–31.3% of q_e is compensated by co-ion/counter-ion exchange. In the positive pore, the co-ion/counter-ion exchange mechanism plays a dominant role (55.2%–

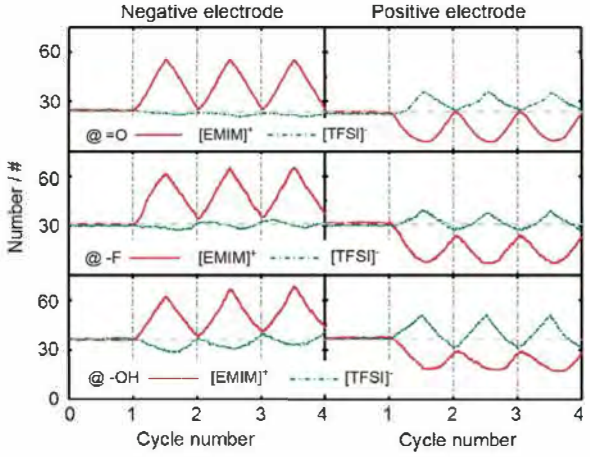

Figure 4. Evolution of the $[EMIM]^+$ and $[TFSI]^-$ ion populations inside the pores for both the negative and positive electrodes during the neutral cycle (0–1 cycle) and the galvanostatic charge–discharge cycles (1–4 cycles).

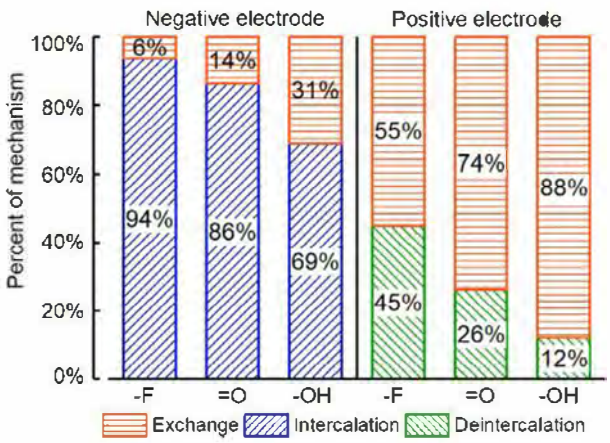

Figure 5. Proportion of each storage mechanism (counter-ion intercalation, co-ion deintercalation, and co-ion/counter-ion exchange) at the negative and positive electrodes when the system is fully charged.

87.9%) in compensating extra electrode charge, and the remaining extra charge (12.1%–44.8%) is compensated by the co-ion deintercalation mechanism.

The change of in-pore ion numbers directly affects the in-pore electrolyte volumes because of the nearly incompressibility of ionic liquids. Assuming a constant occupied volume for the $[EMIM]^+$ and $[TFSI]^-$ ions (see Figure 2c), denoted as $v_+^n = 0.194\ nm^3$ and $v_-^n = 0.239\ nm^3$, respectively, the in-pore ionic volume $v_{ionic}^{in\ pore}$ can be calculated using Equation (1):

$$v_{ionic}^{in\ pore} = n_+^{in\ pore} \times v_+^n + n_-^{in\ pore} \times v_-^n \quad (1)$$

and the total ion number $n_T^{in\ pore}$ is calculated using Equation (2):

$$n_T^{in\ pore} = n_+^{in\ pore} + n_-^{in\ pore} \quad (2)$$

The calculated in-pore ionic volume change of both electrodes is shown in Figure 6, a similar trend is obtained for the evolution of the total ion number $n_T^{in\ pore}$ (see Figure S4 in the Supporting Information). The change of the in-pore ionic volume during charge/ discharge cycles is consistent with the variation of the extra charge on the electrode. The volume change is mainly driven by the counter-ion $[EMIM]^+$ population change, independent of the surface groups present at the surface of the MXene layers. In the positive electrode, the in-pore ionic volume change is more complex to interpret. During charging, below roughly 50% state of charge mainly a co-ion deintercalation mechanism occurs (see Figure 4) in –F- and =O-containing pores; as a result, the total-ion number and ionic volume decrease. Beyond 50% state of charge, the instantaneous intercalation rate of counter-ion $[TFSI]^-$ is faster than the instantaneous deintercalation rate of $[EMIM]^+$, resulting in an increase of the total-ion number and ionic volume. For the –OH-containing surface groups, the ion-swapping mechanism (about 88% ion exchange) leads to a constant ion number and ionic volume change during the first charge.

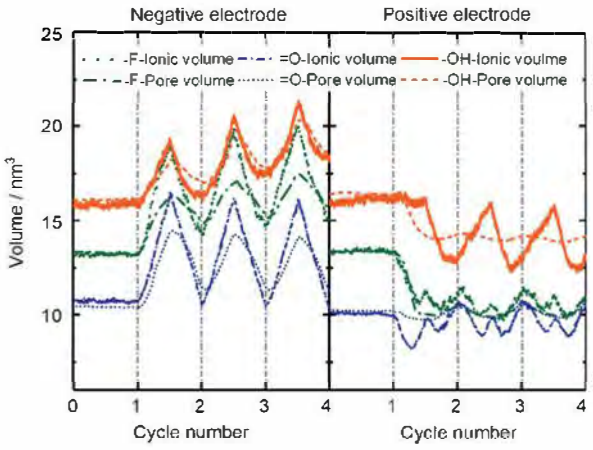

Figure 6. Change of electrode pore volume (dashed line) and in-pore ionic volume (solid line) in both negative and positive electrode pores during the OCV period (0–1 cycle) and galvanostatic charge–discharge cycles (1–4 cycles).

Then, the co-ion deintercalation and counter-ion intercalation is consistent with a volume expansion/contraction during charge–discharge processes. Note that beyond 50% state of discharge the co-ion population is below that present at OCV, resulting in a constant—or slight decrease—of the ionic volume.

The change of in-pore ionic volume and the pore volume between the $Ti_3C_2T_x$ layers present a similar trend in both neutral state and charge–discharge processes. However, some deviations can be seen, especially at the positive electrode. These deviations imply that although the ionic-volume variation caused by the ion intercalation/deintercalation in the MXene electrode dominates the pore/electrode volume variation, other steric effects caused by ionic rearrangement and reorientation cannot be neglected.

Ion arrangement in MXene pores

Beyond the ionic intercalation/deintercalation mechanism occurring during the charge–discharge process, ion arrangement affects the volumetric dynamic of the electrode. Under the action of an electrostatic force, the polar $[EMIM]^+$ and $[TFSI]^-$ molecules will rotate, screening the external electric field. Snapshots of the ionic arrangements inside one of the MXene (here $Ti_3C_2F_2$) electrode pores at different charged states (negatively charged, neutral, and positively charged) are shown in Figure 7. It can be clearly observed that in the negative pore the hydrogen atoms are attracted by the negative surface and prefer to stay near the electrode surface, whereas in the positive pore the oxygen atoms prefer to be located close to the electrode surface. When the electrode is back to the neutral state, the ionic arrangements return to a uniform random arrangement.

To quantitatively analyze the ionic arrangements inside the MXene electrode, the (number) density distributions of $[EMIM]^+$ and $[TFSI]^-$ perpendicular to the $Ti_3C_2T_x$ layer were examined. Figure 8 represents the change of the $[EMIM]^+$ and $[TFSI]^-$ organization and the charge-density distributions in both negative and positive pores under polarization as the simulation proceeds. The ionic distribution undergoes a dynamic reorganization under the external electric field, which favors the screening of the electrostatic interactions. In the negative pore, the $[EMIM]^+$ density distribution changes from only one peak in the middle of the pore at OCV to three peaks as the ionic number and interlayer distance change during the charge–discharge process, in agreement with a counter-ion intercalation charge storage mechanism. At the same time, the co-ion $[TFSI]^-$ density in the negative electrode decreases, moves away from the charged electrode surface, and accumulates in the middle of the interlayer spacing. In the positive pore, the density distribution of the $[TFSI]^-$ counter ion changes from one peak at OCV to two peaks near the electrode surface. The intensity of the peak varies with the amount of extra charge during charge–discharge, but the peak position does not shift. The peak intensity of the co-ion $[EMIM]^+$ increases and decreases upon cycling, in agreement with an ion-exchange mechanism.

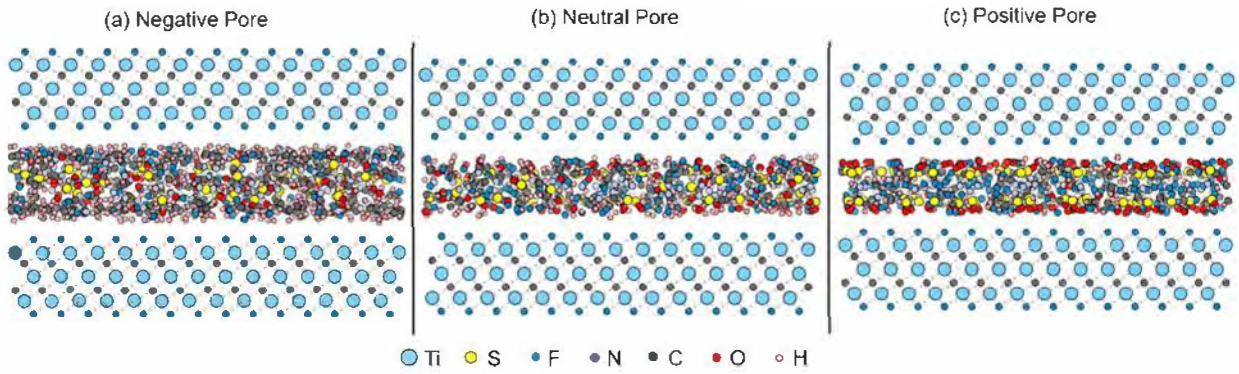

Figure 7. Snapshots of the ionic arrangements inside one of the $Ti_3C_2F_2$ electrode pores at different charged state: (a) negatively charged, (b) neutral, and (c) positively charged, respectively.

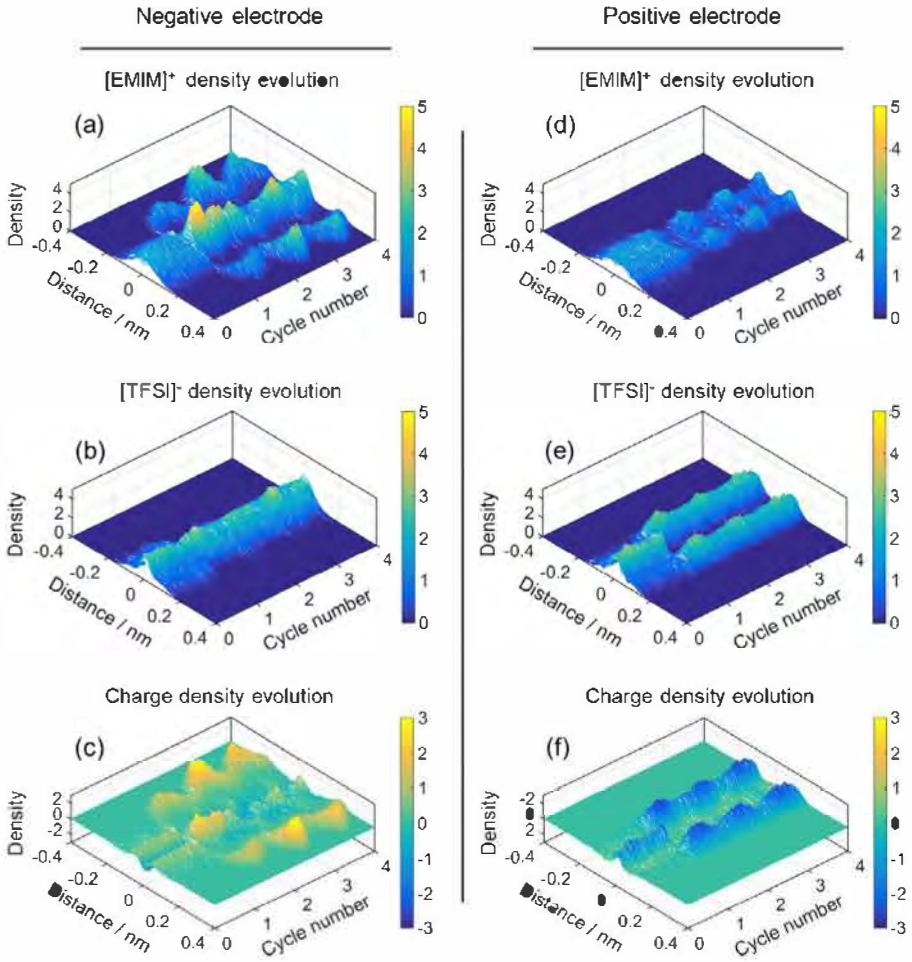

Figure 8. Evolution of $[EMIM]^+$, $[TFSI]^-$ density profiles and charge-density profiles inside the negative electrode pore [(a), (b), (c)] and positive electrode pore [(d), (e), (f)] of $Ti_3C_2F_2$ electrode during neutral cycle (0–1 cycle) and charge–discharge cycle (1–4 cycle), as an example.

Conclusions

We have studied the charge storage mechanism in $Ti_3C_2T_x$ MXene electrodes in contact with a neat 1-ethyl-3-methylimidazolium bis(trifluoromethylsulfonyl)imide ($[EMIM]^+[TFSI]^-$) electrolyte using molecular dynamics simulations. We used parallel MXene layers with different surface groups and applied constant charges on these layers to model charging and discharging. Our molecular simulations reproduce the volume changes of both the negative and positive electrodes observed experimentally. By tracking the ionic number and structural rearrangements inside the pores, we showed that different

charge-storage mechanisms occur at the negative electrode and at the positive electrode. In the negative electrode, the charge storage is mainly achieved by a counter-ion intercalation process whereas an ion-exchange (co-ion deintercalation and counter-ion intercalation) process is observed at the positive electrode. As a result, the total in-pore ion number increases in the negative electrode and decreases in the positive electrode during the charging process. The ionic-number variation correlates well with the dynamic volume changes observed experimentally: a volume expansion is seen on the negative electrode side while there is a contraction on the positive electrode side.

The as-obtained atomistic perspective into the volumetric dynamic and charge storage mechanism of 2D layered nanomaterials can help us design strategies for long lifetime electrodes with limited—or even inexistent—volumetric change. This would allow supercapacitor or actuator applications with controllable deformation. We could select the appropriate electrolyte ions to reduce the deformation. Ions with similar dynamic and geometric properties or bicationic/bianionic electrolytes may be possible strategies to achieve these aims. Considering the limited parameters employed in this modelling work, we can expect that the electrode deformation mechanism might vary if a more realistic electrode structure, the movement pattern of the electrode, and more complex ion–surface interactions (employing a polarizable force field for the ions, for example) are fully taken into account. Also, limited by the chemical nature of the MXenes electrodes (consisting of different atoms: C, O, H, F, and Ti) and the fact that the electrodes can move, we did not employ the constant-potential method here. Previous studies have provided a detailed comparison between the constant-potential method and the constant-charge method and found that these two methods yield essentially similar electric double layer structures, with some deviations for the ion concentrations in the pores being observed.[23] The system studied then was an aqueous electrolyte (2.0 M NaCl electrolyte) in contact with graphene nanopores. The deviations observed in this case may be mitigated by the large amount of ions present in the pure ionic liquid investigated here. Strategies to include the constant potential method in simulations of MXenes will be investigated in the future. Nonetheless, our approach provides significant insights into the microscopic processes occurring during charging and discharging and provides a method to probe different electrolytes in MXene-based supercapacitor systems. We hope that the promising interest on control and utilization of this electrode deformation effect will invite more systematic experimental validations and further theoretical exploration.

Computational Methods

All MD simulations are performed using the LAMMPS software.[24] The NVT (constant number of particles, volume and temperature) ensemble with a target temperature of 450 K was utilized in the simulations. The Verlet leapfrog algorithm with a time step of 1 fs was utilized to integrate Newton's equation of motion. The long-range electrostatic interactions are calculated through the particle–particle–particle-mesh Ewald Scheme. The OPLS-AA force field,[25] the validity of which was verified in previous studies,[26] was used to determine the interactions between the atoms and molecules. A cutoff radius for the van der Waals interactions was set to 1.0 nm. The force-field parameters and simulation model are summarized in the Supporting Information.

During the galvanostatic charge–discharge process, each simulation cycle contained a 0.15 ns charging period and 0.15 ns discharging period. Although these simulation times may seem short, we checked on some selected systems that four times longer simulations (0.6 ns charging and 0.6 ns discharging) give the same results. We believe that this is caused by the small length of the pores (compared to experiments) and to the relatively high temperature used in the simulations (450 K), which leads to fast diffusion of the ions. The charge current density was set to 200 kA cm^{-2}. To acquire reliable statistics, three galvanostatic charge–discharge cycles were performed in one simulation and each simulation case was repeated three times with independent initial configurations. A more detailed discussion of the simulation process and the validity of the simulation system can be found in our previous study.[17f]

Acknowledgements

Kui Xu is supported by China Scholarship Council. This research work is supported by National Natural Science Foundation of China (Grant No. 51302097 & No. 51571096).

Conflict of interest

The authors declare no conflict of interest.

Keywords: ionic liquids · molecular dynamics · nanopores · supercapacitors · two-dimensional materials

[1] D. P. Dubal, O. Ayyad, V. Ruiz, P. Gomez-Romero, *Chem. Soc. Rev.* **2015**, *44*, 1777–1790.

[2] F. Bonaccorso, L. Colombo, G. Yu, M. Stoller, V. Tozzini, A. C. Ferrari, R. S. Ruoff, V. Pellegrini, *Science* **2015**, *347*, 1246501.

[3] G. Zhang, H. Liu, J. Qu, J. Li, *Energy Environ. Sci.* **2016**, *9*, 1190–1209.

[4] a) B. Mendoza-Sánchez, Y. Gogotsi, *Adv. Mater.* **2016**, *28*, 6104–6135; b) B. Anasori, M. R. Lukatskaya, Y. Gogotsi, *Nat. Rev. Mater.* **2017**, *2*, 16098.

[5] a) M. R. Lukatskaya, O. Mashtalir, C. E. Ren, Y. Dall'Agnese, P. Rozier, P. L. Taberna, M. Naguib, P. Simon, M. W. Barsoum, Y. Gogotsi, *Science* **2013**, *341*, 1502–1505; b) O. Mashtalir, M. Naguib, V. N. Mochalin, Y. Dall'Agnese, M. Heon, M. W. Barsoum, Y. Gogotsi, *Nat. Commun.* **2013**, *4*, 1716; c) M. Acerce, D. Voiry, M. Chhowalla, *Nat. Nanotechnol.* **2015**, *10*, 313–318.

[6] a) J. Come, J. M. Black, M. R. Lukatskaya, M. Naguib, M. Beidaghi, A. J. Rondinone, S. V. Kalinin, D. J. Wesolowski, Y. Gogotsi, N. Balke, *Nano Energy* **2015**, *17*, 27–35; b) Z. Lin, P. Rozier, B. Duployer, P.-L. Taberna, B. Anasori, Y. Gogotsi, P. Simon, *Electrochem. Commun.* **2016**, *72*, 50–53.

[7] M. Ghidiu, M. R. Lukatskaya, M. Q. Zhao, Y. Gogotsi, M. W. Barsoum, *Nature* **2014**, *516*, 78–81.

[8] J. M. Griffin, A. C. Forse, W. Y. Tsai, P. L. Taberna, P. Simon, C. P. Grey, *Nat. Mater.* **2015**, *14*, 812–819.

[9] A. C. Forse, J. M. Griffin, C. Merlet, J. Carretero-Gonzalez, A. Rahman, O. Raji, N. M. Trease, C. P. Grey, *Nat. Energy* **2017**, *2*, 16216.

[10] a) W. Y. Tsai, P. L. Taberna, P. Simon, *J. Am. Chem. Soc.* **2014**, *136*, 8722–8728; b) M. D. Levi, M. R. Lukatskaya, S. Sigalov, M. Beidaghi, N. Shpigel, L. Daikhin, D. Aurbach, M. W. Barsoum, Y. Gogotsi, *Adv. Energy Mater.*

2015, *5*, 1400815; c) M. D. Levi, L. Daikhin, D. Aurbach, V. Presser, *Electrochem. Commun.* **2016**, *67*, 16–21.
[11] M. Naguib, V. N. Mochalin, M. W. Barsoum, Y. Gogotsi, *Adv. Mater.* **2014**, *26*, 992–1005.
[12] M. Naguib, O. Mashtalir, J. Carle, V. Presser, J. Lu, L. Hultman, Y. Gogotsi, M. W. Barsoum, *ACS Nano* **2012**, *6*, 1322–1331.
[13] a) X. Wang, X. Shen, Y. Gao, Z. Wang, R. Yu, L. Chen, *J. Am. Chem. Soc.* **2015**, *137*, 2715–2721; b) J. Wen, X. Zhang, H. Gao, *Phys. Chem. Chem. Phys.* **2017**, *19*, 9509–9518; c) H.-W. Wang, M. Naguib, K. Page, D. J. Wesolowski, Y. Gogotsi, *Chem. Mater.* **2016**, *28*, 349–359.
[14] a) Z. Lin, D. Barbara, P.-L. Taberna, K. L. Van Aken, B. Anasori, Y. Gogotsi, P. Simon, *J. Power Sources* **2016**, *326*, 575–579; b) Y. Dall'Agnese, P. Rozier, P.-L. Taberna, Y. Gogotsi, P. Simon, *J. Power Sources* **2016**, *306*, 510–515.
[15] a) O. Mashtalir, M. R. Lukatskaya, M. Q. Zhao, M. W. Barsoum, Y. Gogotsi, *Adv. Mater.* **2015**, *27*, 3501–3506; b) M. Naguib, J. Halim, J. Lu, K. M. Cook, L. Hultman, Y. Gogotsi, M. W. Barsoum, *J. Am. Chem. Soc.* **2013**, *135*, 15966–15969.
[16] N. Jäckel, B. Kruner, K. L. Van Aken, M. Alhabeb, B. Anasori, F. Kaasik, Y. Gogotsi, V. Presser, *ACS Appl. Mater. Interfaces* **2016**, *8*, 32089–32093.
[17] a) C. Péan, C. Merlet, B. Rotenberg, P. A. Madden, P. L. Taberna, B. Daffos, M. Salanne, P. Simon, *ACS Nano* **2014**, *8*, 1576–1583; b) C. Merlet, B. Rotenberg, P. A. Madden, P. L. Taberna, P. Simon, Y. Gogotsi, M. Salanne, *Nat. Mater.* **2012**, *11*, 306–310; c) C. Merlet, C. Pean, B. Rotenberg, P. A. Madden, B. Daffos, P. L. Taberna, P. Simon, M. Salanne, *Nat. Commun.* **2013**, *4*, 2701; d) C. Pean, B. Rotenberg, P. Simon, M. Salanne, *Electrochim. Acta* **2016**, *206*, 504–512; e) V. Ivanistsev, K. Kirchner, T. Kirchner, M. V. Fedorov, *J Phys Condens Matter* **2015**, *27*, 102101; f) K. Xu, X. Ji, B. Zhang, C. Chen, Y. Ruan, L. Miao, J. Jiang, *Electrochim. Acta* **2016**, *196*, 75–83.
[18] a) J. Vatamanu, D. Bedrov, *J. Phys. Chem. Lett.* **2015**, *6*, 3594–3609; b) R. Burt, G. Birkett, X. S. Zhao, *Phys. Chem. Chem. Phys.* **2014**, *16*, 6519–6538; c) D. Bedrov, J. Vatamanu, Z. Hu, *J. Non-Cryst. Solids* **2015**, *407*, 339–348; d) K. Xu, X. Ji, C. Chen, H. Wan, L. Miao, J. Jiang, *Electrochim. Acta* **2015**, *166*, 142–149; e) S. R. Varanasi, S. K. Bhatia, *J. Phys. Chem. C* **2015**, *119*, 17573–17584; f) G. Ori, C. Massobrio, A. Pradel, M. Ribes, B. Coasne, *Langmuir* **2015**, *31*, 6742–6751.
[19] W. Humphrey, A. Dalke, K. Schulten, *J Mol Graph* **1996**, *14*, 33–38.
[20] a) M. A. Hope, A. C. Forse, K. J. Griffith, M. R. Lukatskaya, M. Ghidiu, Y. Gogotsi, C. P. Grey, *Phys. Chem. Chem. Phys.* **2016**, *18*, 5099–5102; b) J. Halim, K. M. Cook, M. Naguib, P. Eklund, Y. Gogotsi, J. Rosen, M. W. Barsoum, *Appl. Surf. Sci.* **2016**, *362*, 406–417.
[21] A. Aksimentiev, K. Schulten, *Biophys. J.* **2005**, *88*, 3745–3761.
[22] A. C. Forse, C. Merlet, J. M. Griffin, C. P. Grey, *J. Am. Chem. Soc.* **2016**, *138*, 5731–5744.
[23] J. Yang, Z. Bo, H. Yang, H. Qi, J. Kong, J. Yan, K. Cen, *ChemElectroChem* **2017**, *4*, 2486–2493.
[24] S. Plimpton, *J. Comput. Phys.* **1995**, *117*, 1–19.
[25] W. L. Jorgensen, D. S. Maxwell, J. Tirado-Rives, *J. Am. Chem. Soc.* **1996**, *118*, 11225–11236.
[26] a) E. Paek, A. J. Pak, G. S. Hwang, *J. Electrochem. Soc.* **2012**, *160*, A1–A10; b) E. Paek, A. J. Pak, G. S. Hwang, *J. Chem. Phys.* **2015**, *142*, 024701.

Manuscript received: October 30, 2017
Accepted manuscript online: December 6, 2017
Version of record online: January 25, 2018